PHYSICAL REVIEW APPLIED **13,** 044036 (2020)

Parametric Amplification of Magnons in Synthetic Antiferromagnets

A. Kamimaki,[1,2] S. Iihama,[2,3] K.Z. Suzuki,[2,3] N. Yoshinaga,[2,4] and S. Mizukami[2,3,5,*]

[1] *Department of Applied Physics, Tohoku University, Aoba 6-6-05, Sendai, 980-8579, Japan*
[2] *WPI AIMR, Tohoku University, Katahira 2-1-1, Sendai, 980-8577, Japan*
[3] *CSRN, Tohoku University, Sendai, 980-8577, Japan*
[4] *MathAM-OIL, AIST, Sendai, 980-8577, Japan*
[5] *CSIS (CRC), Tohoku University, Sendai, 980-8577, Japan*

(Received 13 November 2019; revised manuscript received 31 January 2020; accepted 18 March 2020; published 14 April 2020)

We demonstrate the parametric amplification of an acoustic magnon mode induced by an optical magnon mode in synthetic antiferromagnets, which was achieved by using the all-optical pump-probe time-resolved magneto-optical Kerr effect. The acoustic and optical modes with low and high frequencies, respectively, are clearly observed under different field directions and pump-laser powers. For a relatively high laser power, the acoustic mode shows a temporal increase in amplitude in the time domain; this is observed when the acoustic mode frequency is approximately half the frequency of the optical mode. Correspondingly, we also observe a large enhancement in the spectral density of the acoustic mode in the frequency domain. These data are supported by a numerical simulation using a macrospin model; furthermore, the optical mode amplitude threshold for achieving the acoustic mode amplification is also discussed. The parametric effect in synthetic antiferromagnets demonstrated here can be applied to nanoscale parametric amplifiers and oscillators of magnons, which are the building blocks for spintronic and magnonic computing beyond von Neumann architectures.

DOI: 10.1103/PhysRevApplied.13.044036

I. INTRODUCTION

Exploration of energy-efficient spontaneous oscillation of magnetization and/or magnon amplification is of fundamental and technological interest for utilization in numerous applications, such as neuromorphic architectures [1] and magnonic majority logic gates [2]. Such nonlinear dynamics are typically approached with use of an electric-current-induced spin torque [3–7] and a nonlinear magnon process such as three-magnon splitting [8,9]. The latter process was first explored in Suhl's studies of the second-order instability in ferromagnets (FMs) [10,11]. In this phenomenon, *two spatially nonuniform* magnons with certain energies $\hbar\omega/2$ and momentums $\pm\hbar k$ are formed by the annihilation of *one spatially uniform* ($\hbar k = 0$) magnon with energy $\hbar\omega$; however, this is observed only when the amplitude of the latter magnon is larger than a certain threshold [10]. Thus far, such parametric excitation and amplification of ferromagnetic magnons has been widely investigated in ferromagnets of various shapes, such as slabs, thin films, strips, and disks [12–18].

In this article, we report the parametric amplification of a magnon in a synthetic antiferromagnet (AFM). A synthetic AFM is a stacked layer of FM_1/nonmagnet (NM)/FM_2, which is a useful structure for antiferromagnetic spintronics [19]. The synthetic AFMs investigated in this study have easy-plane magnetic anisotropy due to the large magnetization B_s in each ferromagnetic layer. The antiparallel state of the two magnetization unit vectors $\mathbf{m}_1$ and $\mathbf{m}_2$ for FM_1 and FM_2 is stabilized by an effective magnetic field B_{ex} due to interlayer coupling via the NM. Because a synthetic AFM has two magnetizations, it exhibits acoustic and optical magnon modes, as studied before [20,21]. When a relatively weak external magnetic field B_0 is applied along the in-plane x direction [Figs. 1(a) and 1(b)], it induces a canted state with a net magnetization vector $\mathbf{m} \equiv (\mathbf{m}_1 + \mathbf{m}_2)/2$ parallel to the x axis at equilibrium. $\mathbf{m}$ precesses *about* the x axis in the acoustic mode with a lower frequency [Fig. 1(a)] and oscillates *along* the x axis in the optical mode with a higher frequency [Fig. 1(b)]. These modes are analogous to the ferromagnetic and antiferromagnetic resonances, which arise from the in-phase and out-of-phase precessions of $\mathbf{m}_1$ and $\mathbf{m}_2$, respectively. These linear dynamics in the canted state were examined using coupled macrospin equations of $\mathbf{m}$ and $\mathbf{n} \equiv (\mathbf{m}_1 - \mathbf{m}_2)/2$ [21]. Herein we demonstrate that amplification via nonlinear interaction of these *two spatially uniform* acoustic and optical magnon modes is possible, which enables us to realize magnon amplification using synthetic AFMs on the nanoscale.

---

[*] shigemi.mizukami.a7@tohoku.ac.jp

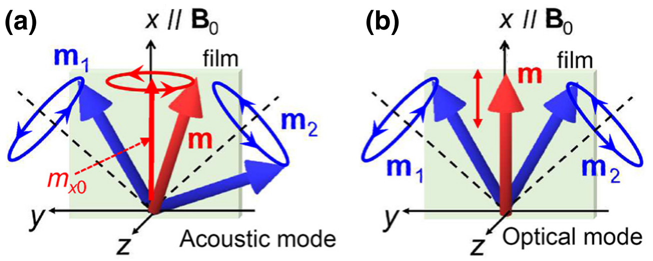

FIG. 1. (a) Acoustic and (b) optical modes for a synthetic AFM. The z axis is parallel to the normal to the film. An external magnetic field B_0 is applied parallel to the x axis. $\mathbf{m}_1$ ($\mathbf{m}_2$) is the magnetization unit vector for ferromagnetic layer 1 (2), and $\mathbf{m} \equiv (\mathbf{m}_1 + \mathbf{m}_2)/2$. m_{x0} is the x component of $\mathbf{m}$ at equilibrium.

II. SIMPLE THEORETICAL ANALYSIS

To gain insight into the physics of the parametric amplification in this study, we approximately derive the equations beyond the linear regime in the large-B_s limit and under the application of an in-plane magnetic field B_0, as shown in Fig. 1.

We consider the free energy F for the synthetic AFMs expressed as

$$F = \sum_{j=1}^{2}\left[-M_sB_0\mathbf{x}\cdot\mathbf{m}_j + \frac{1}{2}M_sB_s\left(\mathbf{m}_j\cdot\mathbf{z}\right)^2\right] + \frac{J_{\mathrm{ex}}}{d_{\mathrm{FM}}}\mathbf{m}_1\cdot\mathbf{m}_2, \tag{1}$$

where $M_s = \mu_0^{-1}B_s$, J_{ex} (greater than 0) is the antiferromagnetic interlayer exchange coupling constant, and d_{FM} is the magnetic layer thickness. B_{ex} is given as $B_{\mathrm{ex}} = J_{\mathrm{ex}}/M_sd_{\mathrm{FM}}$. In the polar coordinate system, the following equations corresponding to the Landau-Lifshitz-Gilbert equations are generally obtained [22,23]:

$$\frac{d\theta_j}{dt} = -\gamma\frac{1}{M_s\sin\theta_j}\frac{\partial F}{\partial\phi_j} - \gamma\alpha_0\frac{1}{M_s}\frac{\partial F}{\partial\theta_j}, \tag{2}$$

$$\sin\theta_j\frac{d\phi_j}{dt} = \frac{\gamma}{M_s}\frac{\partial F}{\partial\theta_j} - \gamma\alpha_0\frac{1}{M_s\sin\theta_j}\frac{\partial F}{\partial\phi_j}, \tag{3}$$

with $\mathbf{m}_j = (\cos\phi_j\sin\theta_j, \sin\phi_j\sin\theta_j, \cos\theta_j)$. Here γ is the gyromagnetic ratio and α_0 is the Gilbert damping constant for the FM. We consider the case where the easy-plane magnetic anisotropy is very strong, $B_0 < 2B_{\mathrm{ex}} \ll B_s$. Then we obtain coupled second-order differential equations from Eqs. (1)–(3) with the approximation of $\theta_j \simeq \pi/2$ using a method similar to that in Ref. [22]:

$$\frac{d^2\phi_m}{dt^2} = -\gamma^2B_0B_s\cos\phi_n\sin\phi_m - \alpha_0\gamma B_s\frac{d\phi_m}{dt}, \tag{4}$$

$$\frac{d^2\phi_n}{dt^2} = -\gamma^2B_0B_s\cos\phi_m\sin\phi_n + \gamma^2B_{\mathrm{ex}}B_s\sin 2\phi_n - \alpha_0\gamma B_s\frac{d\phi_n}{dt}, \tag{5}$$

where we introduce the variables $\phi_m = (\phi_1 + \phi_2)/2$ and $\phi_n = (\phi_1 - \phi_2)/2$. We consider the Taylor series of the small deviations around the equilibrium values, which are expressed as $\phi_m(t) \simeq \delta\phi_m(t)$ and $\phi_n(t) \simeq \phi_{n0} + \delta\phi_n(t)$. Then the following equations for the acoustic and optical modes are obtained from Eqs. (4) and (5) with the lowest order of the nonlinear cross (mode-mixing) term for the acoustic mode (see Appendix A for details):

$$\frac{d^2\delta m_y}{dt^2} = -\omega_{\mathrm{ac}}^2\left(1 + m_{x0}^{-1}\delta m_x\right)\delta m_y - \frac{2}{\tau_{\mathrm{ac}}}\frac{d\delta m_y}{dt}, \tag{6}$$

$$\frac{d^2\delta m_x}{dt^2} = -\omega_{\mathrm{op}}^2\delta m_x - \frac{2}{\tau_{\mathrm{op}}}\frac{d\delta m_x}{dt}, \tag{7}$$

respectively. Some quantities are transformed into those in x-y-z coordinates with use of the following definitions: $m_{x0} = \cos\phi_{n0}$, $n_{y0} = \sin\phi_{n0}$, $\delta m_x = -\delta\phi_n\sin\phi_{n0}$, and $\delta m_y = \delta\phi_m\cos\phi_{n0}$. Here the equilibrium angle of the canted state ϕ_{n0} is determined by the relation $\cos\phi_{n0} \equiv B_0/2B_{\mathrm{ex}}$. The angular frequencies of the two modes are expressed as

$$\omega_{\mathrm{ac}} = 2\pi f_{\mathrm{ac}} = m_{x0}\gamma\sqrt{2B_{\mathrm{ex}}B_s}, \tag{8}$$

$$\omega_{\mathrm{op}} = 2\pi f_{\mathrm{op}} = n_{y0}\gamma\sqrt{2B_{\mathrm{ex}}B_s}. \tag{9}$$

Finally, the relaxation times of the two modes are expressed as

$$1/\tau_{\mathrm{ac}} = 1/\tau_{\mathrm{op}} = \alpha_0\gamma B_s/2. \tag{10}$$

The higher-order terms in Eqs. (6) and (7) are disregarded because we discuss an initial process of the parametric amplification of the acoustic mode by the optical mode in this study.

When the optical mode amplitude δm_x is small enough, the nonlinear cross term $\delta m_x\delta m_y$ in Eq. (6) is negligible and the two modes are decoupled. The value of m_{x0} increases as the magnetic field increases, which implies that the canted state gradually changes to a parallel state [Fig. 1(a)]. This change causes a linear increase in the acoustic mode frequency ω_{ac} [Eq. (8)], as shown in Fig. 2. On the other hand, the optical mode frequency ω_{op} decreases as the magnetic field increases via a decrease in n_{y0} [Eq. (9)], as shown in Fig. 2. In the large-B_s limit, the relaxation times for the two modes are identical [Eq. (10)]; however, they are generally different.

When the optical mode amplitude δm_x is not small enough, the nonlinear cross term $\delta m_x\delta m_y$ in Eq. (6) starts

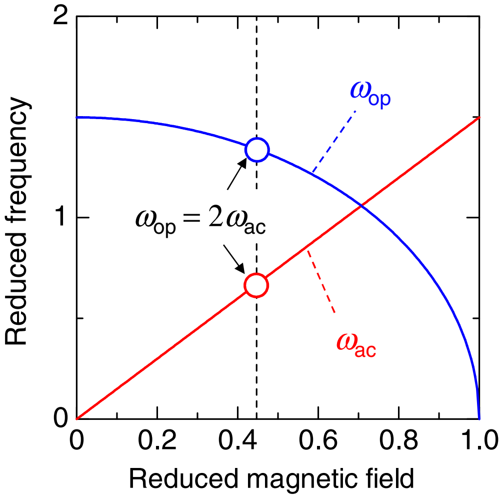

FIG. 2. Theoretical frequencies of the acoustic mode ω_{ac} and the optical mode ω_{op} as a function of the magnetic field B_0 for the in-plane-magnetized synthetic AFM in the large-B_s limit. The data for the acoustic and optical modes are calculated with Eqs. (8) and (9), respectively, with $B_s/2B_{ex} \simeq 2.2$. The frequency and magnetic field are reduced by $\gamma 2B_{ex}$ and $2B_{ex}$, respectively. The dashed line denotes the magnetic field, on which the condition of $\omega_{op} = 2\omega_{ac}$ is satisfied.

playing an important role. Indeed, Eq. (6) for the acoustic mode is the Mathieu equation that predicts a parametric instability. Therefore, Eqs. (6) and (7) predict a parametric instability of the acoustic mode that is induced by the optical mode. This is the mathematical analog of a suspended pendulum with periodically changing length [24]. Here we assume that a certain magnetic field is applied so as to satisfy the condition of $\omega_{op} = 2\omega_{ac}$, as denoted in Fig. 2 by the dashed line. We also consider that the optical mode is continuously excited by an external torque, and then δm_x is expressed as

$$\delta m_x = \delta m_{x0} \cos 2\omega_{ac} t, \tag{11}$$

where δm_{x0} is the oscillation amplitude of the optical mode. Substituting Eq. (11) into Eq. (6), one can find the solution for the oscillation amplitude of the acoustic mode δm_{y0}, which is proportional to the exponential factor [24]

$$\exp\left[\left(-1/\tau_{ac} + \omega_{ac} m_{x0}^{-1} \delta m_{x0}/4\right) t\right]. \tag{12}$$

Equation (12) indicates that the relaxation time of the acoustic mode apparently increases and becomes negative as the optical mode amplitude δm_{x0} increases. This apparent negative relaxation time corresponds to the acoustic mode instability or amplification, which occurs when the optical mode amplitude δm_{x0} overcomes a threshold determined by the following relation:

$$1/\tau_{ac} - \omega_{ac} m_{x0}^{-1} \delta m_{x0}/4 \leq 0. \tag{13}$$

In transient dynamics, the optical mode is not continuously excited and its amplitude decays exponentially, such as $\exp(-t/\tau_{op})$. Even in this case, Eqs. (12) and (13) are approximately valid, because the decay of the optical mode amplitude is much slower than its oscillation frequency. Thus, the amplification may be observed for some duration during which the optical mode amplitude δm_{x0} is larger than the threshold. The acoustic mode grows exponentially in the initial process [Eq. (12)] but eventually its amplitude is saturated by higher-order nonlinear terms, which is not described above. It should also be noted that the above-mentioned parametric amplification is unique to synthetic AFMs, because the nonlinear cross term in Eq. (6) vanishes when the exchange coupling J_{ex} is of the ferromagnetic type (see Appendix A for details).

Although the basic physics of the parametric amplification in this study is understood as mentioned above, the theoretical expressions described in this section are derived for in-plane-magnetized synthetic AFMs in the large-B_s limit. Thus, we also describe a more-general case that is based on the macrospin models for synthetic AFMs to achieve the simulation and analysis of the experimental data, as found in Appendixes B and C, respectively.

III. EXPERIMENTAL METHODS

The dynamics are investigated with an all-optical pump-probe technique in which transient dynamics are induced by the pump pulse and detected by the delayed probe pulse via the magneto-optical Kerr effect [25–28]. We use the standard optical technique with a Ti:sapphire pulsed laser and a regenerative amplifier, as used in previous studies [29,30]. The output laser wavelength, pulse width, and repetition rate are approximately 800 nm, approximately 120 fs, and 1 kHz, respectively. The spot diameter of the pump (probe) laser is approximately 1.1 mm (0.12 mm.) The incident angle of the probe beam is approximately 5°, and the measured Kerr rotation angle is proportional to the z component of the magnetization vectors [Fig. 3(a)]. The film stacking is $\mathrm{Ta(3\,nm)/Fe_{60}Co_{20}B_{20}(3\,nm)/Ru(0.4\,nm)/Fe_{60}Co_{20}B_{20}(3\,nm)/Ta(3\,nm)}$, which is deposited by magnetron sputtering on thermally oxidized Si substrates. $B_s \simeq 1.57$ T and B_{ex} of approximately 0.4 T for the sample are evaluated from magnetization measurements at room temperature using vibrating-sample magnetometers. The magnetizations for the sample are also measured with a physical property measurement system (PPMS) at 300–400 K.

To achieve parametric amplification conditions while maintaining a sufficiently large signal-to-noise ratio for both modes, we measure the dynamics while systematically varying the magnetic field angle θ_B under fixed B_0 of 0.32 T for different pump-laser powers P [Fig. 3(a)]. In this case, the out-of-plane component of B_0 is significantly smaller than the out-of-plane saturation field

$B_{\mathrm{sat}} = 2B_{\mathrm{ex}} + B_s$ for the synthetic AFM in this study, so the magnetizations for the synthetic AFM are nearly in the film plane, as depicted in Fig. 3(a). Consequently, the magnetic field B_0 in the relations for the mode frequencies given by Eqs. (8) and (9) is approximately regarded as its in-plane component; that is, $B_0 \sin\theta_B$ (see Appendix C for details). By changing θ_B, we vary the mode frequencies via the change in the in-plane component of the magnetic field, as discussed in Sec. II. Therefore, the condition $\omega_{\mathrm{op}} = 2\omega_{\mathrm{ac}}$ is satisfied at a certain angle θ_B.

IV. EXPERIMENTAL RESULTS AND DISCUSSION

Figures 3(b)–3(m) display the time-domain data recorded at typical values of θ_B for various values of P. The laser-induced changes in the Kerr rotation angle $\Delta\phi_K$ in the figures are normalized at the saturation value of the polar Kerr rotation angle ϕ_{K0}. For most of the angles, the data show damped periodic changes with different frequencies [Figs. 3(b)–3(e) and 3(j)–3(m)]. These are the weighted sums of the acoustic and optical modes that are excited by the pump pulse and subsequently decay with damping. On the other hand, for the data at angles of approximately 45°–60°, the oscillation amplitudes show nonmonotonic decays [Figs. 3(f)–3(i)]. In this case, the amplitude first increases within 0.1–0.2 ns and then decreases for 10 mW at 45° [Fig. 3(i)]. This behavior becomes less pronounced with decreasing P [Figs. 3(f)–3(h)].

Figures 4(a)–4(d) show the spectral densities (SDs) of $|\Delta\phi_K/\phi_{K0}|$ in the frequency f domain as a function of the angle θ_B for different pump-laser powers P. The SDs are obtained with use of a fast Fourier transform of the time-domain data for $\Delta\phi_K/\phi_{K0}$. The bright and less-intense curves are attributed to the acoustic and optical modes, respectively. The experimental θ_B variations of f_{ac} and f_{op} are qualitatively consistent with being proportional to $\sin\theta_B$ and show no significant change in n_{y0} under relatively small B_0, as described in Secs. II and III. Figures 4(e)–4(h) and 4(i)–4(l) display the absolute detuning $|f_{\mathrm{op}} - 2f_{\mathrm{ac}}|$ and SDs obtained from the two mode peak positions and heights in the frequency-domain data, respectively. The condition $f_{\mathrm{op}} \simeq 2f_{\mathrm{ac}}$ is achieved at a certain magnetic field angle, and we define this angle as θ_c, as shown in Figs. 4(e)–4(h). At $f_{\mathrm{op}} \simeq 2f_{\mathrm{ac}}$, the SDs for the acoustic mode increase remarkably for the 7- and 10-mW data, which correspond to the time-domain data shown in Figs. 3(h) and 3(i), respectively.

To understand the amplitude behavior of the two modes in the time and frequency domains, we simulate the dynamics using a numerical integration of the coupled macrospin equations for **m** and **n** in the thin-NM limit [21] (see also Appendix B):

$$\frac{d\mathbf{m}}{dt} = -\gamma\,\mathbf{m}\times[\mathbf{B}_0 - B_s(\mathbf{m}\cdot\mathbf{z})\mathbf{z}] + \gamma B_s(\mathbf{n}\cdot\mathbf{z})\mathbf{n}\times\mathbf{z} + \alpha_0\left(\mathbf{m}\times\frac{d\mathbf{m}}{dt} + \mathbf{n}\times\frac{d\mathbf{n}}{dt}\right), \tag{14}$$

$$\frac{d\mathbf{n}}{dt} = -\gamma\,\mathbf{n}\times[\mathbf{B}_0 - B_s(\mathbf{m}\cdot\mathbf{z})\mathbf{z} - 2B_{\mathrm{ex}}\mathbf{m}] + \gamma B_s(\mathbf{n}\cdot\mathbf{z})\mathbf{m}\times\mathbf{z} + (\alpha_0 + \alpha_{\mathrm{sp}})\left(\mathbf{m}\times\frac{d\mathbf{n}}{dt} + \mathbf{n}\times\frac{d\mathbf{m}}{dt}\right) - \alpha_{\mathrm{sp}}\left[\frac{1}{m^2}\mathbf{m}\cdot\left(\mathbf{n}\times\frac{d\mathbf{m}}{dt}\right)\mathbf{m} + \frac{1}{n^2}\mathbf{n}\cdot\left(\mathbf{m}\times\frac{d\mathbf{n}}{dt}\right)\mathbf{n}\right], \tag{15}$$

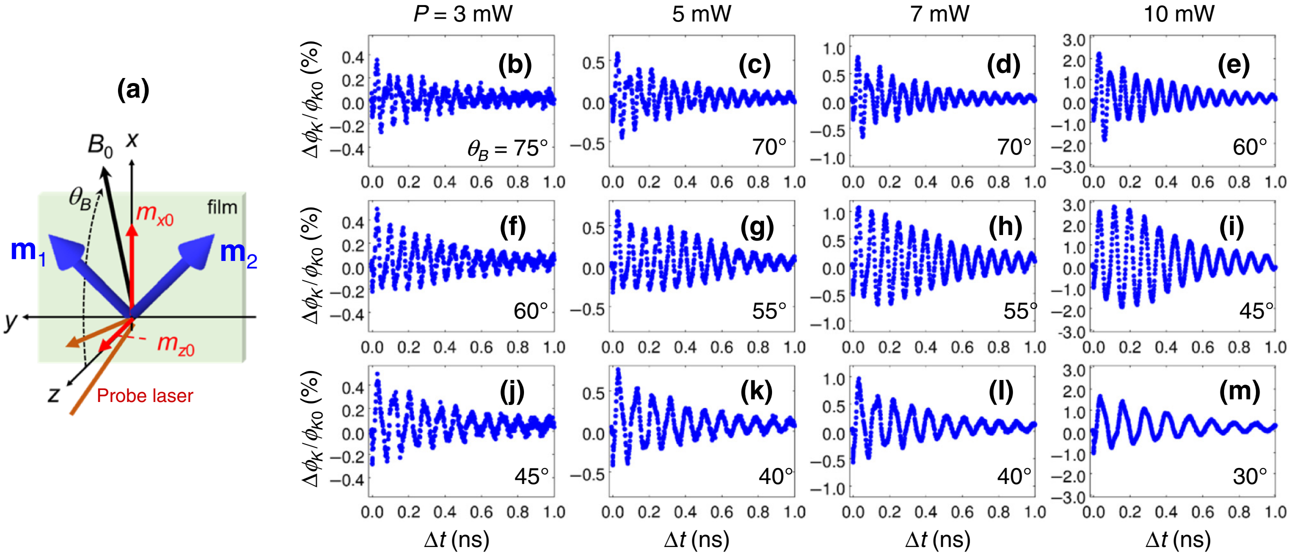

FIG. 3. (a) The coordinate system for the optical measurement. The field angle θ_B is measured relative to the film normal (z axis). (b)–(m) Normalized laser-induced change in the Kerr rotation angle $\Delta\phi_K/\phi_{K0}$ versus delay time Δt measured at typical θ_B values for different pump-laser powers P.

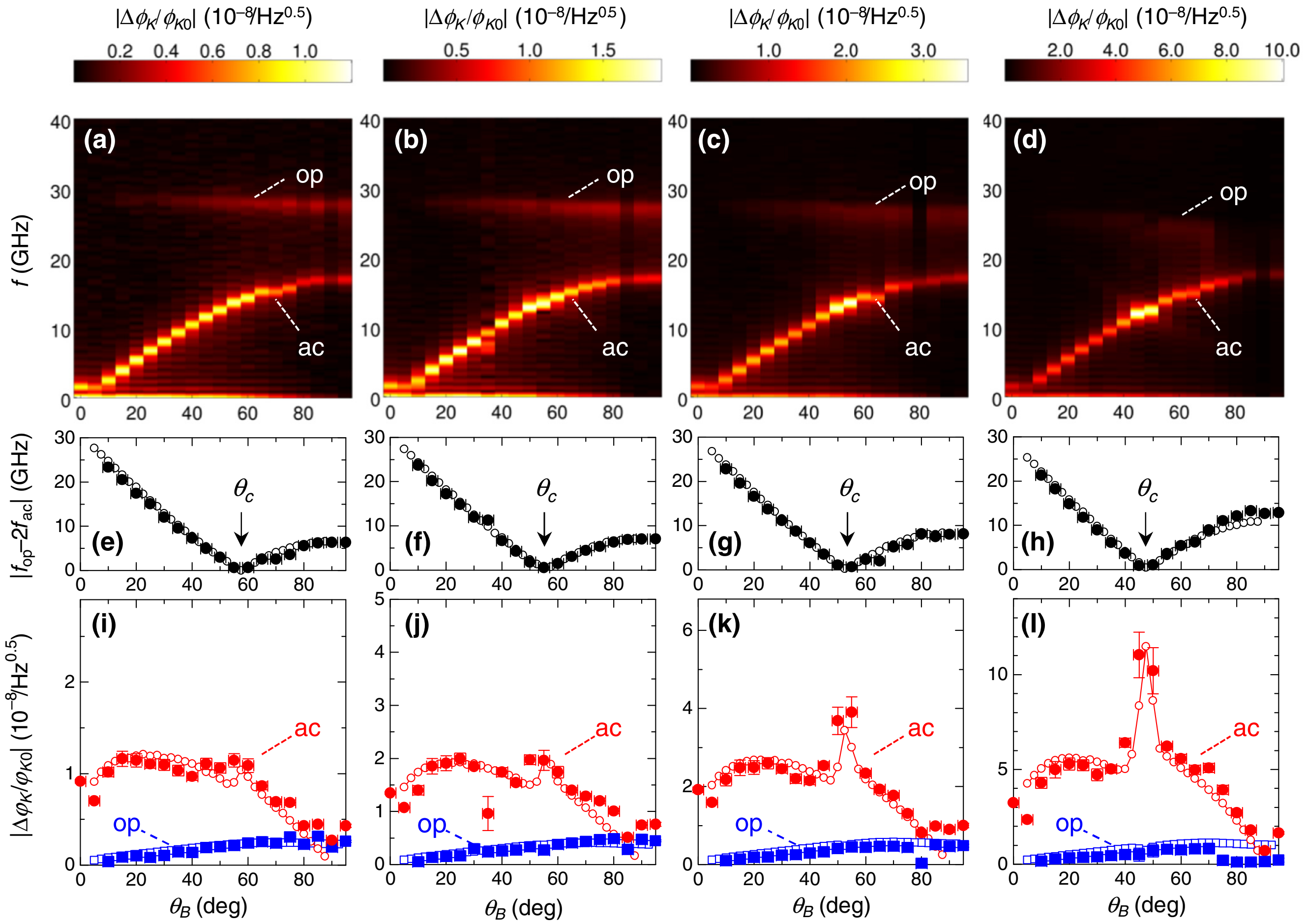

FIG. 4. (a)–(d) SDs of the laser-induced change in the Kerr rotation angle $\Delta\phi_K/\phi_{K0}$ as functions of the frequency f and the field angle θ_B. θ_B variation of (e)–(h) the absolute detuning $|f_{\text{op}} - 2f_{\text{ac}}|$ and (i)–(l) the SDs for the acoustic (ac; circles) and optical (op; squares) modes. The solid and open symbols denote the experimental and simulated data, respectively. (a),(e),(i) for P of 3 mW; (b),(f),(j) for 5 mW; (c),(g),(k) for 7 mW; and (d),(h),(l) for 10 mW. θ_c in (e)–(h) denotes the field angle θ_B at which f_{op} is equal to $2f_{\text{ac}}$.

where α_{sp} is the additional Gilbert damping constant due to the spin-pumping effect [31]. The laser-induced changes in the effective fields are phenomenologically modeled, as explained below. Ultrafast demagnetization and recovery [26,32] are taken into account with use of the relation $B_s(t) = B_{s0} - \Delta B_s c(t)$, with the mean value B_{s0} and reduction at the zero delay ΔB_s. The temporal change used in Ref. [33] is approximated as

$$c(t) = (1 - c_0)e^{-t/\tau} + \frac{c_0}{\sqrt{t/t_0 + 1}} \quad (t \geq 0), \tag{16}$$

where the first and second terms represent rapid and slow recoveries, respectively. These recoveries are characterized by the amplitude constant c_0 (≤ 1), picosecond relaxation time τ, and relatively long heat-diffusion time t_0. The initial femtosecond-to-subpicosecond change is simplified as a step function. B_{ex} also decreases with rising temperature [34,35], so the relation $B_{\text{ex}}(t) = B_{\text{ex0}} - \Delta B_{\text{ex}} c(t)$ is also used similarly to its use in previous studies [36,37]. Here B_{ex0} and ΔB_{ex} are defined similarly to $B_s(t)$. Our simulation focuses on the dynamics on a timescale of hundreds of picoseconds and is irrelevant to the details of microscopic modeling [26,38,39], which takes into account the femtosecond-to-picosecond dynamics of electron, spin, and lattice temperatures. The observed quantity is computed with use of the relation

$$\frac{\Delta\phi_K}{\phi_{K0}} = \left[1 - \frac{\Delta B_s}{B_{s0}} c(t)\right] [m_z(t) + r_{mn} n_z(t)] - m_{z0}, \tag{17}$$

where r_{mn} (much less than 1) is the ratio of the Kerr rotation angle of n_z and m_z, which stems from the two magnetic layers located at different depths [40] (see also Appendix D for details).

The data obtained in the simulation using reasonable parameters (see Table I and its legend) are similar to the experimental data [Figs. 4(i)–4(l)]. The broad θ_B variations of the simulated SDs originate from the θ_B variation of m_{x0}, m_{z0}, and the magnitude of the laser-induced torques.

TABLE I. The parameters used in the simulation. We use $\gamma/2\pi = 29.5$ GHz/T, $B_{s0} = 1.57$ T, $\alpha_0 = 0.01$, $\alpha_{\rm sp} = 0.01$, $\tau = 1.5$ ps, $t_0 = 30$ ps, and $r_{mn} = -0.065$ for any P values. $\Delta B_s/B_{s0}$, c_0, τ, and t_0 are obtained from the time-domain data below the 20-ps regime (see Appendix E). γ, α_0, and $\alpha_{\rm sp}$ are evaluated with use of the experimental data at 3 mW (see Appendix F). $B_{\rm ex0}$ is determined by our fitting the detuning values in Figs. 4(e)–4(h). $\Delta B_{\rm ex}$ and r_{mn} are obtained by our fitting the SDs in Figs. 4(i)–4(l).

P (mW)	$B_{\rm ex0}$ (T)	$\Delta B_{\rm ex}/B_{\rm ex0}$	$\Delta B_s/B_{s0}$	c_0
3	0.355	0.075	0.028	0.58
5	0.350	0.12	0.042	0.59
7	0.340	0.16	0.055	0.61
10	0.325	0.29	0.11	0.66

The sharp peaks of the simulated SDs near θ_c are caused by the nonlinear mode coupling. The slight change in the simulated θ_c with increasing P is due to the reduction of $f_{\rm op}$ via that of $B_{\rm ex0}$ (Table I) [see Eq. (9)]. This $B_{\rm ex0}$ reduction indicates a rise in the time-averaged temperature under laser illumination for higher P. A similar reduction in $B_{\rm ex}$ is observed at a temperature slightly higher than room temperature in our magnetization measurements (see Appendix G).

Figures 5(a)–5(d) and 5(e)–5(h) show the simulated time-domain data in the vicinity of θ_c at different powers P for the laser-induced change in the Kerr rotation angle $\Delta\phi_K/\phi_{K0}$ and the corresponding optical mode δm_x ($\equiv m_x - m_{x0}$), respectively. Initial increases in the amplitude of $\Delta\phi_K/\phi_{K0}$ on the negative sides are observed in Figs. 5(c) and 5(d), as indicated by arrows, which well capture the experimental observations in Figs. 3(h) and 3(i).

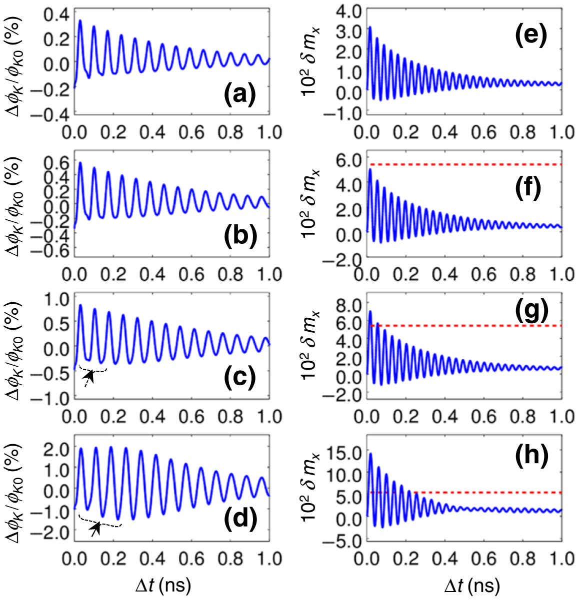

FIG. 5. Simulated time-domain data. Laser-induced change in the Kerr rotation angle $\Delta\phi_K/\phi_{K0}$ for (a) 57.5° at 3 mW, (b) 55.0° at 5 mW, (c) 52.5° at 7 mW, and (d) 47.5° at 10 mW. (e)–(h) The corresponding optical mode amplitude δm_x. The dashed lines in (f),(g),(h) denote the threshold $\delta m_{x0,c}$. The arrows denote increases in the amplitude.

As discussed at the end of Sec. II, such initial increases can be observed for some duration where the optical mode amplitude δm_{x0} is larger than the threshold. To evaluate the threshold, we extend the nonlinear theory described in Sec. II to the more-general case with the weak magnetic field applied obliquely (see Appendix C for details). Then we obtain approximate analytical expressions for the threshold as well as the mode frequencies and relaxation times. The threshold in the present case is derived from the instability condition at $f_{\rm op} = 2f_{\rm ac}$, given by

$$\delta m_{x0,c} = \frac{1}{1-p^{-2}}\frac{4m_{x0}}{\omega_{\rm ac}\tau_{\rm ac}}, \tag{18}$$

with the acoustic mode frequency

$$\omega_{\rm ac} = 2\pi f_{\rm ac} = p\gamma B_0 \sin\theta_B \tag{19}$$

and its relaxation time:

$$1/\tau_{\rm ac} = \alpha_0\gamma B_{\rm ex}[m_{x0}^2 + p^2(1-m_{z0}^2)]. \tag{20}$$

Here m_{x0} and m_{z0} are the x and z components of $\mathbf{m}$ at equilibrium, respectively [Fig. 3(a)],

$$m_{x0} = (B_0/2B_{\rm ex})\sin\theta_B, \tag{21}$$

$$m_{z0} = p^{-2}(B_0/2B_{\rm ex})\cos\theta_B, \tag{22}$$

and p is the acoustic mode ellipticity,

$$p = (1 + B_s/2B_{\rm ex})^{1/2}. \tag{23}$$

Equations (19)–(21) become identical to the corresponding equations described in Sec. II when we set the large-B_s limit and $\theta_B = 90°$ in Eqs. (19)–(21).

We estimate the threshold $\delta m_{x0,c} \simeq 0.054$ from Eqs. (18)–(23) with the parameters in this study, as shown in Figs. 5(f)–5(h) by the dashed lines. Initial increases in the amplitude of $\Delta\phi_K/\phi_{K0}$ [Figs. 5(c) and 5(d)] occur when δm_x moves across the threshold [Figs. 5(g) and 5(h)]. Therefore, the initial temporal increase in the amplitude [Figs. 3(h) and 3(i)] and the sharp peaks of the SD [Figs. 4(k) and 4(l)] for the experimental data at 7 and 10 mW are evidence of parametric amplification of the acoustic mode. The optical mode amplitude in the simulated 3- and 5-mW data is smaller than the threshold [Figs. 5(e) and 5(f)] and, therefore, the small increase in the simulated SDs in the vicinity of θ_c [Figs. 4(i) and 4(j)] may be understood as an effective increase in the acoustic mode relaxation time due to nonlinear interactions that is not large enough to overcome the threshold. A more-quantitative discussion of the threshold requires further investigations that are beyond the scope of this study.

Finally, it is worthwhile commenting on the possibility of observing the amplification in synthetic AFMs by means of the conventional radio-frequency (rf) technique. In the three-magnon-splitting or subsidiary absorption experiments in ferromagnets, as described at the beginning of Sec. I, the rf magnetic field is applied perpendicular to the direction of the static magnetic field. When the magnitude of the rf magnetic field exceeds the threshold, parametric instability of ferromagnetic magnons occurs. This threshold depends on the sizes, shapes, and material parameters of ferromagnets. Typical values for the threshold of the rf magnetic field were reported as approximately 0.1–0.6 mT for thick permalloy films [12] and approximately 1–3 mT in strip-shaped permalloy films [17]. In the case of synthetic AFMs, the optical mode can be excited when the rf magnetic field is applied parallel to the direction of the static magnetic field, so-called longitudinal pumping [20]. The typical threshold of the rf magnetic field for the synthetic AFMs is evaluated as about 1.5 mT for the present synthetic AFM sample when the optical mode is resonantly excited by longitudinal pumping (see Appendix H for details). This threshold is comparable to the above-mentioned value in strip-shaped permalloy films [17]. Thus, the parametric amplification in synthetic AFMs can be observed with a rf setup similar to that in Ref. [17].

V. SUMMARY AND OUTLOOK

We investigate the dynamics of acoustic and optical magnon modes in synthetic AFMs with the all-optical pump-probe technique. We clearly observe acoustic and optical modes with low and high frequencies for different field directions and pump-laser powers. We find that the acoustic mode amplitudes temporally increase in the time domain at a relatively high laser power P and $f_{\mathrm{op}} \simeq 2f_{\mathrm{ac}}$. Correspondingly, large enhancements in the SDs are also observed in the frequency domain. These are characteristics of parametric amplification of the acoustic magnon mode induced by the optical magnon mode. The numerical simulation using the macrospin model well explain the experimental frequency-domain and time-domain data, and we also discuss the threshold necessary to realize the amplification.

As mentioned in Sec. I, a parametric amplifier or oscillator is one of the fundamental building blocks to develop computers beyond von Neumann architectures. One interesting device concept is the magnonic majority logic gate, in which the phases of ferromagnetic magnons are used as the information encoded into the inputs and the parametric amplifier of ferromagnetic magnons is used for nonlinear bistable phase elements [2]. This is a magnonic parametron in a modern sense, being analogous to the parametron using ferrite cores invented in the past [41]. Similarly, one can design a synthetic-AFM-based magnonic parametron by utilizing the parametric amplification of the acoustic magnon mode. Synthetic AFMs show relatively strong nonreciprocity in magnon propagation [42–45], so the synthetic-AFM-based magnonic parametron could have an input or output isolation better than that of the ferromagnet-based one. In addition, our study naturally suggests that synthetic AFMs also work as parametric nano-oscillators. Nano-oscillators play a major role in some types of modern reservoir computing. Such computing architecture is being extensively studied using nanoscale dc-biased spin-torque oscillators (STOs) [1,46] and large numbers of arrays of nano-STOs [47]. The auto-oscillation of the acoustic modes in synthetic AFMs can be driven by the wireless rf magnetic field via optical mode pumping. Thus, synthetic-AFM-based oscillator arrays are free from complicated wiring issues and simple and low-cost integrations would be possible. The above-mentioned threshold of the rf magnetic field can be reduced by a factor of about 100 in the case of synthetic AFMs composed of low-damping magnets with α_0 of about 0.001 or less [48–52]. Therefore, an energy-efficient nanoamplifier or nano-oscillator of magnons is feasible.

ACKNOWLEDGMENTS

A.K. acknowledges the Graduate Program in Spintronics (GP-Spin) at Tohoku University A.K. and S.M. thank K. Saito for his technical support. S.M. thanks H. Kurebayashi and Y. Nozaki for valuable discussions. This work was supported in part by KAKENHI (Grants No. 26103004 and No. 19K15430), CSRN, and ATP of WPI-AIMR.

APPENDIX A: SOME DETAILS OF THE ANALYSIS IN SEC. II

In Eqs. (4) and (5), we consider the Taylor series of the small deviations around the equilibrium values, which are expressed as $\phi_m(t) \simeq \delta\phi_m(t)$ and $\phi_n(t) \simeq \phi_{n0} + \delta\phi_n(t)$. Then the following equations are obtained with the lowest order of the nonlinear cross (mode-mixing) terms:

$$\frac{d^2\delta\phi_m}{dt^2} = -\gamma^2 B_0 B_s \cos\phi_{n0}\left(1 - \frac{\sin\phi_{n0}}{\cos\phi_{n0}}\delta\phi_n\right)\delta\phi_m - \alpha_0\gamma B_s\frac{d\delta\phi_m}{dt}, \tag{A1}$$

$$\frac{d^2\delta\phi_n}{dt^2} = -\gamma^2 2B_{\mathrm{ex}}B_s\sin^2\phi_{n0}\left(1 - \frac{1}{2}\frac{\cos^2\phi_{n0}}{\sin^2\phi_{n0}}\delta\phi_m^2\right)\delta\phi_n + \frac{1}{2}\gamma^2 B_0 B_s\sin\phi_{n0}\delta\phi_m^2 - \alpha_0\gamma B_s\frac{d\delta\phi_n}{dt}. \tag{A2}$$

By transforming some quantities into those in the x-y-z coordinates, as performed in Sec. II, we obtain Eqs. (6)

and (7), as follows:

$$\frac{d^2\delta m_y}{dt^2} = -\omega_{\mathrm{ac}}^2\left(1+m_{x0}^{-1}\delta m_x\right)\delta m_y - \frac{2}{\tau_{\mathrm{ac}}}\frac{d\delta m_y}{dt}, \tag{A3}$$

$$\begin{aligned}\frac{d^2\delta m_x}{dt^2} &= -\omega_{\mathrm{op}}^2\left(1-\frac{1}{2}n_{y0}^{-2}\delta m_y^2\right)\delta m_x - \frac{1}{2}\omega_{\mathrm{ac}}^2 n_{y0}^2 m_{x0}^{-3}\delta m_y^2 \\ &\quad - \frac{2}{\tau_{\mathrm{op}}}\frac{d\delta m_x}{dt}, \qquad\qquad (\mathrm{A4}) \\ &\simeq -\omega_{\mathrm{op}}^2\delta m_x - \frac{2}{\tau_{\mathrm{op}}}\frac{d\delta m_x}{dt}. \qquad\qquad (\mathrm{A5})\end{aligned}$$

Here we use the expressions for ω_{ac}, ω_{op}, τ_{ac}, and τ_{op} as in Eqs. (8)–(10). In Eq. (A4), the terms δm_y^2 and $\delta m_x \delta m_y^2$ are negligible when we discuss an initial process of parametric amplification of the acoustic mode by the optical mode in this study. The nonlinear cross term in Eq. (A1) vanishes for the case of ferromagnetic coupling because $\sin\phi_{n0} = 0$, as mentioned in Sec. II.

APPENDIX B: COUPLED MACROSPIN EQUATIONS WITH THE SPIN-PUMPING EFFECT USED IN THIS STUDY

We consider the case where an external magnetic field B_0 is applied in an arbitrary direction. As described in Sec. II, the free energy F is expressed as

$$F = \sum_{j=1}^{2}\left[-M_s B_0 \mathbf{u}\cdot\mathbf{m}_j + \frac{1}{2}M_s B_s\left(\mathbf{m}_j\cdot\mathbf{z}\right)^2\right] + \frac{J_{\mathrm{ex}}}{d_{\mathrm{FM}}}\mathbf{m}_1\cdot\mathbf{m}_2, \tag{B1}$$

where $\mathbf{u}$ is the unit vector for the direction of the external magnetic field. The Landau-Lifshitz-Gilbert equation for the jth ferromagnetic layer without the spin-pumping effect is expressed as

$$\frac{d\mathbf{m}_j}{dt} = -\gamma\mathbf{m}_j\times\mathbf{B}_j + \alpha_0\mathbf{m}_j\times\frac{d\mathbf{m}_j}{dt} \quad (j=1,2). \tag{B2}$$

Here the effective magnetic field $\mathbf{B}_j$ is given as $\mathbf{B}_j = -M_s^{-1}\partial F/\partial\mathbf{m}_j$. From Eqs. (B1) and (B2), the two coupled equations for $\mathbf{m}$ and $\mathbf{n}$ without the spin-pumping effect are derived as

$$\frac{d\mathbf{m}}{dt} = -\Omega_L\mathbf{m}\times\mathbf{u} + \Omega_B\left[(\mathbf{m}\cdot\mathbf{z})\,\mathbf{m}\times\mathbf{z} + (\mathbf{n}\cdot\mathbf{z})\,\mathbf{n}\times\mathbf{z}\right] + \alpha_0\left(\mathbf{m}\times\frac{d\mathbf{m}}{dt} + \mathbf{n}\times\frac{d\mathbf{n}}{dt}\right), \tag{B3}$$

$$\frac{d\mathbf{n}}{dt} = -\Omega_L\mathbf{n}\times\mathbf{u} + \Omega_B\left[(\mathbf{m}\cdot\mathbf{z})\,\mathbf{n}\times\mathbf{z} + (\mathbf{n}\cdot\mathbf{z})\,\mathbf{m}\times\mathbf{z}\right] + 2\Omega_{\mathrm{ex}}\mathbf{n}\times\mathbf{m} + \alpha_0\left(\mathbf{m}\times\frac{d\mathbf{n}}{dt} + \mathbf{n}\times\frac{d\mathbf{m}}{dt}\right), \tag{B4}$$

where we define $\Omega_L = \gamma B_0$, $\Omega_B = \gamma B_s$, and $\Omega_{\mathrm{ex}} = \gamma B_{\mathrm{ex}}$. When the spin-pumping effect is taken into account, extra torque terms are added to Eqs. (B3) and (B4) [21]:

$$\begin{aligned}\mathbf{T}_m &= \alpha_m\left(\mathbf{m}\times\frac{d\mathbf{m}}{dt} + \mathbf{n}\times\frac{d\mathbf{n}}{dt}\right) \\ &\quad + 2\alpha_m\eta\left[\frac{1}{1-\eta(m^2-n^2)}\mathbf{m}\cdot\left(\mathbf{n}\times\frac{d\mathbf{n}}{dt}\right)\mathbf{m} + \frac{1}{1+\eta(m^2-n^2)}\mathbf{n}\cdot\left(\mathbf{m}\times\frac{d\mathbf{m}}{dt}\right)\mathbf{n}\right], \\ \mathbf{T}_n &= \alpha_n\left(\mathbf{m}\times\frac{d\mathbf{n}}{dt} + \mathbf{n}\times\frac{d\mathbf{m}}{dt}\right) \\ &\quad - 2\alpha_n\eta\left[\frac{1}{1+\eta(m^2-n^2)}\mathbf{m}\cdot\left(\mathbf{n}\times\frac{d\mathbf{m}}{dt}\right)\mathbf{m} + \frac{1}{1-\eta(m^2-n^2)}\mathbf{n}\cdot\left(\mathbf{m}\times\frac{d\mathbf{n}}{dt}\right)\mathbf{n}\right],\end{aligned}$$

where some quantities are expressed as

$$\begin{aligned}\alpha_m &= \frac{\alpha_1 g_r}{1+g_r\coth\left(d_{\mathrm{NM}}/2\lambda\right)}, \\ \alpha_n &= \frac{\alpha_1 g_r}{1+g_r\tanh\left(d_{\mathrm{NM}}/2\lambda\right)}, \\ \eta &= \frac{g_r}{\sinh\left(d_{\mathrm{NM}}/\lambda\right) + g_r\cosh\left(d_{\mathrm{NM}}/\lambda\right)}, \\ \alpha_1 &= \gamma\frac{1}{M_s d_{\mathrm{FM}}}\left(\frac{\hbar}{2e}\right)^2(\rho\lambda)^{-1}, \\ g_r &= 2\rho\lambda G_r.\end{aligned}$$

Here d_{NM} is the thickness of the nonmagnetic layer, λ is the spin-diffusion length, η is the back-flow efficiency of the spin current, ρ is the resistivity of the nonmagnetic layer, and G_r is the real part of the mixing conductance for the FM/NM interface. In our case, we take the limit of $d_{\mathrm{NM}}/\lambda \to 0$ because λ in the case where the NM is Ru is larger than d_{NM} of 0.4 nm in this study [53]. Then, the additional damping α_m is ignored, and η is taken as unity. Consequently, we obtain $\mathbf{T}_m = 0$, and $\mathbf{T}_n$ is expressed as

$$\mathbf{T}_n = \alpha_{\mathrm{sp}}\left(\mathbf{m}\times\frac{d\mathbf{n}}{dt} + \mathbf{n}\times\frac{d\mathbf{m}}{dt}\right) - \alpha_{\mathrm{sp}}\times\left[\frac{1}{m^2}\mathbf{m}\cdot\left(\mathbf{n}\times\frac{d\mathbf{m}}{dt}\right)\mathbf{m} + \frac{1}{n^2}\mathbf{n}\cdot\left(\mathbf{m}\times\frac{d\mathbf{n}}{dt}\right)\mathbf{n}\right], \tag{B5}$$

where we use $m^2 + n^2 = 1$ and define the additional damping α_{sp} as

$$\alpha_{\mathrm{sp}} = \gamma \frac{1}{M_s d_{\mathrm{FM}}} \left(\frac{\hbar}{2e}\right)^2 2G_r.$$

The value of α_{sp} is independent of the resistivity of the NM ρ in this case. Equations (B3) and (B4) with Eq. (B5) correspond to Eqs. (14) and (15), respectively.

APPENDIX C: THEORETICAL ANALYSIS FOR THE CASE OF APPLICATION OF A RELATIVELY WEAK OBLIQUE MAGNETIC FIELD

We consider the case where a relatively weak magnetic field is applied in the x-z plane. To obtain some approximate analytical expressions, the vectors $\mathbf{m}$ and $\mathbf{n}$ are expressed as the sum of the equilibrium and time-dependent parts: $\mathbf{m}(t) = \mathbf{m}_0 + \delta\mathbf{m}(t)$ and $\mathbf{n}(t) = \mathbf{n}_0 + \delta\mathbf{n}(t)$. Substituting these quantities into Eqs. (14) and (15) and using the equilibrium conditions, we obtain $\mathbf{m}$ and $\mathbf{n}$ at equilibrium, which are expressed as $\mathbf{m}_0 = m_{x0}\mathbf{x} + m_{z0}\mathbf{z}$ and $\mathbf{n}_0 = n_{y0}\mathbf{y}$. Each component is given as follows:

$$m_{x0} = \frac{B_0}{2B_{\mathrm{ex}}} u_x, \tag{C1}$$

$$m_{z0} = \frac{B_0}{B_s + 2B_{\mathrm{ex}}} u_z, \tag{C2}$$

$$n_{y0} = \sqrt{1 - m_{x0}^2 - m_{z0}^2}, \tag{C3}$$

where $u_x = \sin\theta_B$ and $u_z = \cos\theta_B$ with the magnetic field angle θ_B with respect to the film normal, and the relation $m^2 + n^2 = 1$ is used. Subsequently, from the equation of the first order and second order for δ, we obtain the following six coupled equations:

$$\begin{aligned}\frac{d\delta m_x}{dt} &= \Omega_B n_{y0}\delta n_z - 2\Omega_{\mathrm{ex}} m_{z0}\delta m_y - \alpha_0 m_{z0}\frac{d\delta m_y}{dt} \\ &\quad + \alpha_0 n_{y0}\frac{d\delta n_z}{dt},\end{aligned} \tag{C4}$$

$$\begin{aligned}\frac{d\delta m_y}{dt} &= -\left(\Omega_L u_x + \Omega_B m_{x0}\right)\delta m_z + 2\Omega_{\mathrm{ex}} m_{z0}\delta m_x \\ &\quad - \alpha_0 m_{x0}\frac{d\delta m_z}{dt} + \alpha_0 m_{z0}\frac{d\delta m_x}{dt} - \Omega_B \delta m_x \delta m_z,\end{aligned} \tag{C5}$$

$$\frac{d\delta m_z}{dt} = \Omega_L u_x \delta m_y + \alpha_0 m_{x0}\frac{d\delta m_y}{dt} - \alpha_0 n_{y0}\frac{d\delta n_x}{dt}, \tag{C6}$$

$$\begin{aligned}\frac{d\delta n_x}{dt} &= \left(\Omega_B + 2\Omega_{\mathrm{ex}}\right) n_{y0}\delta m_z - \left(\alpha_0 + \alpha_{\mathrm{sp}}\right) m_{z0}\frac{d\delta n_y}{dt} \\ &\quad + \left(\alpha_0 + \alpha_{\mathrm{sp}}\right) n_{y0}\frac{d\delta m_z}{dt},\end{aligned} \tag{C7}$$

$$\begin{aligned}\frac{d\delta n_y}{dt} &= -\Omega_B m_{x0}\delta n_z - \left(\alpha_0 + \alpha_{\mathrm{sp}}\right) m_{x0}\frac{d\delta n_z}{dt} \\ &\quad + \left(\alpha_0 + \alpha_{\mathrm{sp}}\right) m_{z0}\frac{d\delta n_x}{dt},\end{aligned} \tag{C8}$$

$$\begin{aligned}\frac{d\delta n_z}{dt} &= -2\Omega_{\mathrm{ex}} n_{y0}\delta m_x + \left(\alpha_0 + \alpha_{\mathrm{sp}}\right) m_{x0}\frac{d\delta n_y}{dt} \\ &\quad - \left(\alpha_0 + \alpha_{\mathrm{sp}}\right) n_{y0}\frac{d\delta m_x}{dt}.\end{aligned} \tag{C9}$$

Here we use Eqs. (C1) and (C2) and the definitions of $\Omega_L = \gamma B_0$, $\Omega_B = \gamma B_s$, and $\Omega_{\mathrm{ex}} = \gamma B_{\mathrm{ex}}$, as defined in Appendix B. In Eqs. (C4)–(C9), we take only the term $-\Omega_B \delta m_x \delta m_z$ as a leading nonlinear term, according to the analysis in Appendix A. In Eqs. (C4)–(C9), we drop the last term of Eq. (15) because this term is negligibly small in this study.

In this study, m_{z0} is on the order of 0.1, which is smaller than m_{x0} and n_{y0} for most of the θ_B values. Thus, we solve Eqs. (C4)–(C9) in a perturbative way:

$$\begin{aligned}\delta\mathbf{m}(t) &\simeq \delta\mathbf{m}^{(0)}(t) + m_{z0}\delta\mathbf{m}^{(1)}(t) + m_{z0}^2\delta\mathbf{m}^{(2)}(t) + \cdots, \\ \delta\mathbf{n}(t) &\simeq \delta\mathbf{n}^{(0)}(t) + m_{z0}\delta\mathbf{n}^{(1)}(t) + m_{z0}^2\delta\mathbf{n}^{(2)}(t) + \cdots.\end{aligned}$$

Substituting $\delta\mathbf{m}(t)$ and $\delta\mathbf{n}(t)$ into Eqs. (C4)–(C9), we decouple the six coupled equations [Eqs. (C4)–(C9)] into two sets of three zeroth-order coupled equations for each acoustic and optical mode, except for the nonlinear cross term:

$$\frac{d\delta m_x^{(0)}}{dt} = \Omega_B n_{y0}\delta n_z^{(0)} + \alpha_0 n_{y0}\frac{d\delta n_z^{(0)}}{dt}, \tag{C10}$$

$$\frac{d\delta n_y^{(0)}}{dt} = -\Omega_B m_{x0}\delta n_z^{(0)} - \left(\alpha_0 + \alpha_{\mathrm{sp}}\right) m_{x0}\frac{d\delta n_z^{(0)}}{dt}, \tag{C11}$$

$$\begin{aligned}\frac{d\delta n_z^{(0)}}{dt} &= -2\Omega_{\mathrm{ex}} n_{y0}\delta m_x^{(0)} + \left(\alpha_0 + \alpha_{\mathrm{sp}}\right) m_{x0}\frac{d\delta n_y^{(0)}}{dt} \\ &\quad - \left(\alpha_0 + \alpha_{\mathrm{sp}}\right) n_{y0}\frac{d\delta m_x^{(0)}}{dt}\end{aligned} \tag{C12}$$

for the optical mode, and

$$\begin{aligned}\frac{d\delta m_y^{(0)}}{dt} &= -\left(\Omega_L u_x + \Omega_B m_{x0}\right)\delta m_z^{(0)} - \Omega_B \delta m_x^{(0)}\delta m_z^{(0)} \\ &\quad - \alpha_0 m_{x0}\frac{d\delta m_z^{(0)}}{dt},\end{aligned} \tag{C13}$$

$$\frac{d\delta m_z^{(0)}}{dt} = \Omega_L u_x \delta m_y^{(0)} + \alpha_0 m_{x0}\frac{d\delta m_y^{(0)}}{dt} - \alpha_0 n_{y0}\frac{d\delta n_x^{(0)}}{dt}, \tag{C14}$$

$$\frac{d\delta n_x^{(0)}}{dt} = \left(\Omega_B + 2\Omega_{\mathrm{ex}}\right) n_{y0}\delta m_z^{(0)} + \left(\alpha_0 + \alpha_{\mathrm{sp}}\right) n_{y0}\frac{d\delta m_z^{(0)}}{dt} \tag{C15}$$

for the acoustic mode. Finally, we obtain two coupled second-order differential equations for the optical and acoustic modes from Eqs. (C10)–(C12) and (C13)–(C15), respectively, with the condition that α_0 and $\alpha_{\rm sp}$ are much smaller than unity:

$$\frac{d^2\delta m_x^{(0)}}{dt^2} = -\omega_{\rm op}^2\delta m_x^{(0)} - \frac{2}{\tau_{\rm op}}\frac{d\delta m_x^{(0)}}{dt}, \tag{C16}$$

$$\frac{d^2\delta m_z^{(0)}}{dt^2} = -\omega_{\rm ac}^2\left(1+\epsilon\delta m_x^{(0)}\right)\delta m_z^{(0)} - \frac{2}{\tau_{\rm ac}}\frac{d\delta m_z^{(0)}}{dt}. \tag{C17}$$

Here the acoustic and optical mode angular frequencies are expressed as

$$\omega_{\rm ac} = \sqrt{\Omega_L u_x\left(\Omega_L u_x + \Omega_B m_{x0}\right)}, \tag{C18}$$

$$\omega_{\rm op} = n_{y0}\sqrt{2\Omega_{\rm ex}\Omega_B}. \tag{C19}$$

The relaxation times of the acoustic and optical modes are expressed as

$$\frac{1}{\tau_{\rm ac}} = \frac{1}{2}\alpha_0\left[m_{x0}\left(2\Omega_L u_x + \Omega_B m_{x0}\right) + n_{y0}^2\left(\Omega_B + 2\Omega_{\rm ex}\right)\right], \tag{C20}$$

$$\frac{1}{\tau_{\rm op}} = \frac{1}{2}\alpha_0\left[\Omega_B m_{x0}^2 + \left(\Omega_B + 2\Omega_{ex}\right)n_{y0}^2\right] + \frac{1}{2}\alpha_{\rm sp}\Omega_B\left(m_{x0}^2 + n_{y0}^2\right). \tag{C21}$$

The coupling constant of the acoustic and optical modes ϵ in Eq. (C17) is given as

$$\epsilon = \Omega_L u_x \Omega_B \omega_{\rm ac}^{-2}. \tag{C22}$$

Consequently, the following relation is obtained from Eq. (C17) in a way similar to the description in Sec. II:

$$\frac{1}{\tau_{\rm ac}} - \frac{1}{4}\omega_{\rm ac}\epsilon\delta m_{x0} \le 0. \tag{C23}$$

From Eq. (C23), the threshold is given as

$$\delta m_{x0,c} = \frac{4}{\omega_{\rm ac}\tau_{\rm ac}\epsilon}. \tag{C24}$$

We note that Eqs. (18), (19), (20), (21), and (22) are rewritten using Eqs. (C24), (C18), (C20), (C1), and (C2) with ellipticity p [Eq. (23)], respectively. The ellipticity p of the acoustic mode in the linear regime without damping is derived from Eqs. (C13) and (C18) as

$$p = \left|\frac{\delta m_y^{(0)}}{\delta m_z^{(0)}}\right| = \frac{\Omega_L u_x + \Omega_B m_{x0}}{\omega_{\rm ac}} = \sqrt{1 + \frac{B_s}{2B_{\rm ex}}}. \tag{C25}$$

In the large-B_s limit, $\delta m_y^{(0)}$ is much larger than $\delta m_z^{(0)}$ from Eq. (C25), so the acoustic mode can be approximated as described in Sec. II.

The first-order equations are written as

$$\frac{d\delta m_y^{(1)}}{dt} = -\left(\Omega_L u_x + \Omega_B m_{x0}\right)\delta m_z^{(1)} + 2\Omega_{\rm ex}\delta m_x^{(0)} + \cdots,$$

$$\frac{d\delta m_z^{(1)}}{dt} = \Omega_L u_x \delta m_y^{(1)} + \cdots.$$

These equations mean that the optical mode is hybridized into the acoustic mode as the first-order correction:

$$\delta m_z \simeq m_{z0}\frac{2\Omega_{\rm ex}\Omega_L u_x}{\omega_{\rm ac}^2 - \omega_{\rm op}^2}\delta m_x^{(0)}.$$

Thus, the optical mode has a z component under the application of an oblique magnetic field, the amplitude of which is proportional to m_{z0}. The perturbation corrections for the frequency, the relaxation time, etc. are also inversely proportional to the mode separation in their frequencies $\omega_{\rm op} - \omega_{\rm ac}$. Therefore, as an approximation these corrections are ignored here. This is because B_0 is small enough and no frequency degeneracies for the acoustic and optical modes are observed in this study.

APPENDIX D: SOME DETAILS OF THE MAGNETO-OPTICAL KERR EFFECT

The polar magneto-optical Kerr rotation angle ϕ_K in the synthetic AFMs is the weighted sum of the angles from each ferromagnetic layer. This is proportional to the z component of the magnetization:

$$\phi_K(t) = a_1(t)m_{1z}(t) + a_2(t)m_{2z}(t), \tag{D1}$$

where a_j ($j = 1, 2$) is a proportionality factor that depends not only on the optical and magneto-optical parameters of jth ferromagnetic layer but also on those of other layers [54]. By introducing the quantities $a_m = (a_1 + a_2)/2$ and $a_n = (a_1 - a_2)/2$, we rewrite Eq. (D1) as

$$\phi_K(t) = 2a_m(t)\left[m_z(t) + r_{mn}n_z(t)\right]. \tag{D2}$$

Here we approximate $r_{mn} = a_n/a_m$ as a constant. In the conventional manner, Eq. (D2) is expressed as

$$\phi_K(t) = 2bB_s(t)\left[m_z(t) + r_{mn}n_z(t)\right], \tag{D3}$$

with the constant proportionality factor b. The laser-induced change in the Kerr rotation angle $\Delta\phi_K$ in the experiments is expressed as

$$\begin{aligned}\Delta\phi_K(t) &= \phi_K(t) - \phi_K(-0)\\ &= 2bB_s(t)\left[m_z(t) + r_{mn}n_z(t)\right]\\ &\quad - 2bB_{s0}\left(m_{z0} + r_{mn}n_{z0}\right).\end{aligned} \tag{D4}$$

Using the relations $\phi_{K0} = 2bB_{s0}$ and $n_{z0}(-0) = 0$, we obtain the expression

$$\frac{\Delta\phi_K(t)}{\phi_{K0}} = \frac{B_s(t)}{B_{s0}}\left[m_z(t) + r_{mn}n_z(t)\right] - m_{z0}. \tag{D5}$$

We finally obtain Eq. (17) by substituting $B_s(t) = B_{s0} - \Delta B_s c(t)$ into Eq. (D5).

The very small factor r_{mn} originates from the small difference in the magneto-optical Kerr rotation angle between FM_1 and FM_2 located at different depths [40]. To examine the validity of the r_{mn} value of -0.065 used in the simulations (see the legend for Table I), we perform a numerical calculation of r_{mn} using the standard magneto-optical theory for multilayer films [54,55]. We consider the model stacking of Si substrate/SiO_2(100)/Ta(3 nm)/$Fe_{60}Co_{20}B_{20}$(3 nm)/Ru (0.4 nm)/$Fe_{60}Co_{20}B_{20}$(3)/Ta(1.5 nm)/Ta-O(1.5 nm)/air, where we take into account the oxidation of the Ta capping layer. The literature values of the complex refractive indices for the materials at a light wavelength of 800 nm are used, as shown in Table II. The value of the complex magneto-optical constant Q for $Fe_{60}Co_{20}B_{20}$ at a light wavelength of 800 nm is unknown. Therefore, we evaluate r_{mn} using several values ($-Q' = 0.035 - 0.020$, $Q'' = 0.005 - 0.014$) expected from the values of the complex magneto-optical constant Q for those alloys measured at a light wavelength of approximately 630 nm [56]. The values of r_{mn} are evaluated as 0.04–0.05, meaning that the Kerr rotation angle of the top $Fe_{60}Co_{20}B_{20}$ layer is slightly larger than that of the bottom $Fe_{60}Co_{20}B_{20}$ layer. This value is in rough agreement with the r_{mn} value used in the simulations. The sign of r_{mn} depends on the definition of the positions of FM_1 and FM_2 (i.e., top or bottom) in the macrospin model. Thus, it is irrelevant to the discussion in this study.

APPENDIX E: THE PARAMETERS RELATED TO THE DEMAGNETIZATION AND RECOVERY

Figure 6 shows the time-domain data near zero delay for the synthetic AFM sample measured with a magnetic field of approximately 2 T applied perpendicular to the film plane with different pump-laser powers P. The rapid change of $\Delta\phi_K$ at Δt of about 0 ps is due to the ultrafast demagnetization induced by the pump laser. Subsequently, $\Delta\phi_K$ shows relatively slow change. The curves in Fig. 6 show the calculated data for $c(t)$ obtained with Eq. (16) and are fitted to the experimental data. Here we assume that τ and t_0 are approximately independent of P. From this fitting we obtain τ, t_0, and c_0, as shown in Table I and its legend.

From Eqs. (17), (22), and (23), we obtain the relation for the demagnetization and the magnetic field angle:

$$\frac{\Delta\phi_K\,(t=0)}{\phi_{K0}} = -\frac{\Delta B_s}{B_{s0}}m_{z0} = -\eta_B\cos\theta_B. \tag{E1}$$

Here we define the factor η_B, which is expressed as

$$\eta_B = \frac{\Delta B_s}{B_{s0}}\frac{B_0}{B_{s0} + 2B_{\mathrm{ex}0}}. \tag{E2}$$

Using Eq. (E1), we obtain the η_B value from the experimental data for the θ_B variation of $\Delta\phi_K/\phi_{K0}$ at zero delay measured at 0.32 T for each laser power P. Then we extract

TABLE II. Refractive indices for the materials used in the calculation of the magneto-optical effect for the synthetic AFM sample in this study.

Material	Refractive index	Reference
Ta_2O_5	$2.10 + i0.00128$	[57]
Ta	$1.11 + i3.48$	[58]
Ru	$3.95 + i5.34$ at 633 nm	[59]
$Fe_{60}Co_{20}B_{20}$	$3.40 + i4.30$	[60]
SiO_2	1.45	[61]
Si	$3.68 + i0.0054$	[62]

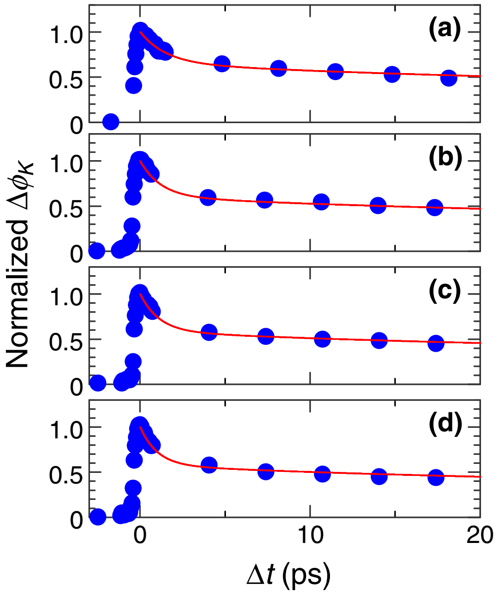

FIG. 6. Time-domain normalized values of the laser-induced change in the Kerr rotation angle $\Delta\phi_K$ near zero delay with a pump-laser power P of (a) 10 mW, (b) 7 mW, (c) 5 mW, and (d) 3 mW. The data are measured with a magnetic field of approximately 2 T applied perpendicular to the film plane. The curves represent the calculated data fitted to the experimental data.

value of $\Delta B_s/B_{s0}$ from the η_B value using the values for B_{ex0} for each laser power P, B_{s0}, and B_0 that are input into the simulation.

APPENDIX F: ANALYSIS OF THE EXPERIMENTAL DATA OBTAINED AT 3 MW IN THE TIME AND FREQUENCY DOMAINS

Figure 7 shows the typical time-domain and frequency-domain data measured at a pump-laser power P of 3 mW. As described earlier, the measured time-domain data are normalized by the saturation Kerr rotation angle. Subsequently, we obtain the SD in the frequency domain using the fast Fourier transform with zero padding [63]. In the absence of both nonlinear effects and large temporal changes in the magnetic moment values, the data can be analyzed by the summation of the following functions for the two modes with a proper offset function, as conventionally performed:

$$\propto e^{-t/\tau_i}\sin(2\pi f_i + \phi_i) \tag{F1}$$

for the time-domain data $\Delta\phi_K(t)/\phi_{K0}$, and

$$\propto \left[(2\pi)^2(f - f_i)^2 + \tau_i^{-2}\right]^{-1/2} \tag{F2}$$

for the frequency-domain data $|\Delta\phi_K(f)/\phi_{K0}|$. Here f_i is the frequency, τ_i is the relaxation time, and ϕ_i is the phase for the acoustic mode ($i =$ ac) or the optical mode ($i =$ op). The results of the fittings using Eqs. (F1) and (F2) are shown in Figs. 7(a) and 7(b), respectively by the solid curves.

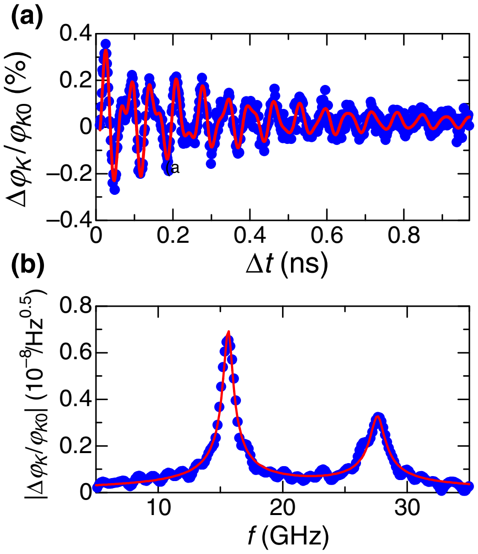

FIG. 7. Typical data obtained with a pump-laser power P of 3 mW at a magnetic field angle θ_B of 75° in the time domain (a) and the frequency domain (b). Solid curves represent the theoretical data and are fitted to the experimental data. The data near zero delay are removed in (a).

Figure 8 displays the frequencies f and relaxation times τ for the acoustic and optical modes as a function of the magnetic field angle θ_B. Here we show the data obtained from the fitting to both the time-domain data and the frequency-domain data. The data for the θ_B dependence of f_{ac}, f_{op}, and $1/\tau_{\mathrm{ac}}$ obtained from the time-domain data are nearly equal to those obtained from the frequency-domain data, as shown in Figs. 8(a) and 8(b). However, there are relatively large uncertainties in the data for the θ_B dependence of $1/\tau_{\mathrm{op}}$, as shown in Fig. 8(c). This is because the z component of the amplitude for the optical mode observed in our measurement is much smaller than that for the acoustic mode. We also show the data calculated using Eqs. (C18)–(C21) with the parameters given in Table I and its legend. The theoretical data for f_{ac} are in accordance with the experimental data for most of the θ_B values [Fig. 8(a)]. The experimental $1/\tau_{\mathrm{op}}$ values are

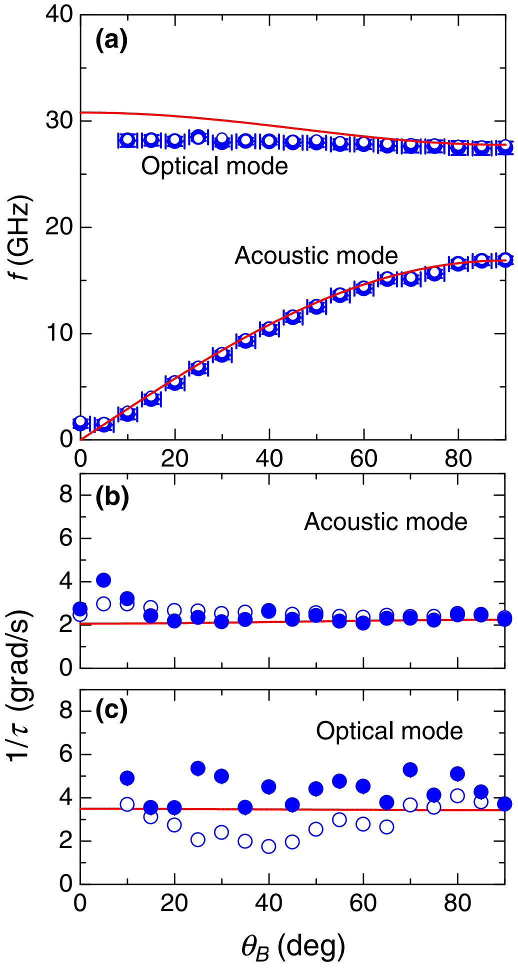

FIG. 8. Dependence of (a) the mode frequencies f and relaxation time τ on the magnetic field angle θ_B for the (b) acoustic mode and the (c) optical mode evaluated with the time-domain data (solid circles) and the frequency-domain data (open circles) measured at a pump-laser power P of 3 mW. Solid curves represent the theoretically calculated data.

approximated by the theoretical values [Fig. 8(c)]. The experimental data for f_{op} and $1/\tau_{\mathrm{ac}}$ slightly and systematically deviate from the theoretical values at $\theta_B \simeq 0^\circ$, as seen in Fig. 8(a) and 8(b), respectively. The increase in the experimental $1/\tau_{\mathrm{ac}}$ values at $\theta_B \simeq 0^\circ$ [Fig. 8(b)] may stem from some magnetic inhomogeneities in the present sample, because a similar behavior is observed in the magnetization dynamics in ferromagnets as an increase of the ferromagnetic resonance linewidth in a low-frequency regime [63]. On the other hand, the inconsistency between the experimental and theoretical data for the f_{op} values [Fig. 8(a)] is not yet clear. This is not due to the approximation accuracy of Eq. (C19) since the exact theoretical values of f_{op} show a difference of only a few percent from the values calculated with Eq. (C19) (not shown here). We believe this discrepancy for f_{op} will not significantly influence the discussion of the parametric amplification in this study, since we focus on the data at θ_B of about 40°–60°, where the theoretical values are not very different from the experimental ones.

The fitting using Eq. (F1) did not work well for the data measured at a magnetic field angle θ_B near θ_c with higher pump-laser powers P. This is because the amplitudes of the optical mode are much smaller than those of the acoustic mode with larger P at $\theta_B \simeq \theta_c$. In addition, the temporal change of the measured Kerr rotation angles for the acoustic mode are very different from Eq. (F1) at larger P, as seen in Figs. 3(g)–3(i), because of the effect of the parametric amplification on its amplitude.

APPENDIX G: TEMPERATURE DEPENDENCE OF THE INTERLAYER COUPLING

Figure 9 shows several values for the effective magnetic field due to the interlayer coupling B_{ex} in the synthetic AFM sample in this study obtained at different temperatures, which are evaluated from the out-of-plane saturation magnetic field B_{sat} with the relation $B_{\mathrm{sat}} = 2B_{\mathrm{ex}} + B_s$. The large reduction of B_{ex} with increasing temperature is similar to that reported in Ref. [35]. We also confirm that the temperature dependence of B_s is negligible in this temperature range.

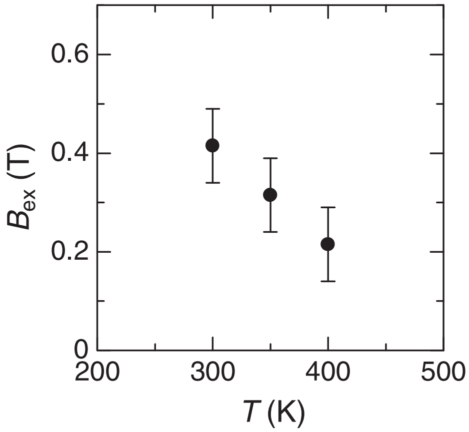

FIG. 9. Effective magnetic field due to the interlayer coupling B_{ex} as a function of the temperature T in the synthetic AFM sample in this study.

APPENDIX H: THE PARAMETRIC AMPLIFICATION IN rf EXPERIMENTS

We consider the in-plane-magnetized synthetic AFM under static magnetic field $B_0\mathbf{x}$ (i.e., $\theta_B = 90^\circ$) and rf microwave magnetic field $\delta b_x(t)\mathbf{x}$; namely, longitudinal pumping [20]. By adding the external torque due to the rf field $\gamma n_{y0}\delta b_x(t)$ to Eq. (C12), we obtain the equation corresponding to Eq. (C16):

$$\frac{d^2\delta m_x}{dt^2} = -\omega_{\mathrm{op}}^2\delta m_x - \frac{2}{\tau_{\mathrm{op}}}\frac{d\delta m_x}{dt} + \Omega_B n_{y0}^2\gamma\delta b_x(t). \quad \text{(H1)}$$

By substituting the sinusoidal rf magnetic field with its frequency tuned to that of the optical mode, $\delta b_x(t) = \delta b_{x0}\sin\omega_{\mathrm{op}}t$, we obtain the sinusoidal solution of the optical mode, such as Eq. (11), from Eq. (H1), whose amplitude δm_{x0} is expressed as

$$\delta m_{x0} = \left(\frac{2}{\tau_{\mathrm{op}}}\omega_{\mathrm{op}}\right)^{-1}\Omega_B n_{y0}^2\gamma\delta b_{x0}, \quad \text{(H2)}$$

where δb_{x0} is the amplitude of the rf magnetic field. With the condition $\omega_{\mathrm{op}} = 2\omega_{\mathrm{ac}}$, we obtain the threshold of the rf-magnetic-field amplitude $\delta b_{x0,c}$ for the parametric amplification of the acoustic mode by substituting Eq. (H2) into Eq. (18):

$$\delta b_{x0,c} = \frac{\Delta\omega_{\mathrm{op}}\Delta\omega_{\mathrm{ac}}}{\gamma\Omega_B}\frac{4}{1-p^{-2}}\frac{m_{x0}}{n_{y0}^2}, \quad \text{(H3)}$$

where $\Delta\omega_{\mathrm{ac}} = 2/\tau_{\mathrm{ac}}$ is the full linewidth of the rf absorption for the acoustic mode and $\Delta\omega_{\mathrm{op}} = 2/\tau_{\mathrm{op}}$ is that for the optical mode in the frequency domain.

For the present synthetic AFM sample with the parameters given in Table I and its legend, $\omega_{\mathrm{op}} = 2\omega_{\mathrm{ac}} \simeq$ 29 GHz is evaluated at $B_0 = 0.27$ T at $\theta_B = 90^\circ$ from Eqs. (C1)–(C3), (C18), and (C19). Under this condition, $\delta b_{x0,c}$ is evaluated as about 1.5 mT from Eq. (H3) with the relaxation times for the acoustic and optical modes evaluated from Eqs. (C20) and (C21).

---

[1] J. Torrejon, M. Riou, F. A. Araujo, S. Tsunegi, G. Khalsa, D. Querlioz, P. Bortolotti, V. Cros, K. Yakushiji, A. Fukushima, H. Kubota, S. Yuasa, M. D. Stiles, and J. Grollier, Neuromorphic computing with nanoscale spintronic oscillators, Nature **547**, 428 (2017).

[2] A. Khitun, M. Bao, and K. L. Wang, Magnonic logic circuits, J. Phys. D. Appl. Phys. **43**, 264005 (2010).

[3] L. Berger, Emission of spin waves by a magnetic multilayer traversed by a current, Phys. Rev. B **54**, 9353 (1996).

[4] J. C. Slonczewski, Current-driven excitation of magnetic multilayers, J. Magn. Magn. Mater. **159**, L1 (1996).

[5] M. Tsoi, A. G. M. Jansen, J. Bass, W.-C. Chiang, V. Tsoi, and P. Wyder, Generation and detection of phase-coherent current-driven magnons in magnetic multilayers, Nature **406**, 46 (2000).

[6] K. Ando, S. Takahashi, K. Harii, K. Sasage, J. Ieda, S. Maekawa, and E. Saitoh, Electric Manipulation of Spin Relaxation Using the Spin-Hall Effect, Phys. Rev. Lett. **101**, 036601 (2008).

[7] H. Fulara, M. Zahedinejad, R. Khymyn, A. A. Awad, S. Muralidhar, M. Dvornik, and J. Akerman, Spin-orbit torque-driven propagating spin waves, Sci. Adv. **5**, eaax8467 (2019).

[8] P. E. Wigen, *Nonlinear Phenomena and Chaos in Magnetic Materials* (World Scientific, Singapore, 1994).

[9] C. L. Ordóñez-Romero, B. A. Kalinikos, P. Krivosik, W. Tong, P. Kabos, and C. E. Patton, Three-magnon splitting and confluence processes for spin-wave excitations in yttrium iron garnet films: Wave vector selective Brillouin light scattering measurements and analysis, Phys. Rev. B **79**, 144428 (2009).

[10] H. Suhl, Subsidiary absorption peaks in ferromagnetic resonance at high signal levels, Phys. Rev. **101**, 1437 (1956).

[11] H. Suhl, The theory of ferromagnetic resonance at high signal powers, J. Phys. Chem. Solids **1**, 209 (1957).

[12] S. Y. An, P. Krivosik, M. A. Kraemer, H. M. Olson, A. V. Nazarov, and C. E. Patton, High power ferromagnetic resonance and spin wave instability processes in permalloy thin films, J. Appl. Phys. **96**, 1572 (2004).

[13] M. Bao, A. Khitun, Y. Wu, J.-Y. Lee, K. L. Wang, and A. P. Jacob, Coplanar waveguide radio frequency ferromagnetic parametric amplifier, Appl. Phys. Lett. **93**, 072509 (2008).

[14] C. W. Sandweg, Y. Kajiwara, A. V. Chumak, A. A. Serga, V. I. Vasyuchka, M. B. Jungfleisch, E. Saitoh, and B. Hillebrands, Spin Pumping by Parametrically Excited Exchange Magnons, Phys. Rev. Lett. **106**, 216601 (2011).

[15] H. Kurebayashi, O. Dzyapko, V. E. Demidov, D. Fang, A. J. Ferguson, and S. O. Demokritov, Controlled enhancement of spin-current emission by three-magnon splitting, Nat. Mater. **10**, 660 (2011).

[16] H. G. Bauer, P. Majchrak, T. Kachel, C. H. Back, and G. Woltersdorf, Nonlinear spin-wave excitations at low magnetic bias fields, Nat. Commun. **6**, 8274 (2015).

[17] G. Okano and Y. Nozaki, Spin waves parametrically excited via three-magnon scattering in narrow NiFe strips, Phys. Rev. B **100**, 104424 (2019).

[18] K. Schultheiss, R. Verba, F. Wehrmann, K. Wagner, L. Korber, T. Hula, T. Hache, A. Kákay, A. A. Awad, V. Tiberkevich, A. N. Slavin, J. Fassbender, and H. Schultheiss, Excitation of Whispering Gallery Magnons in a Magnetic Vortex, Phys. Rev. Lett. **122**, 097202 (2019).

[19] R. A. Duine, K.-J. Lee, S. S. P. Parkin, and M. D. Stiles, Synthetic antiferromagnetic spintronics, Nat. Phys. **14**, 217 (2018).

[20] Z. Zhang, L. Zhou, P. E. Wigen, and K. Ounadjela, Angular dependence of ferromagnetic resonance in exchange-coupled Co/Ru/Co trilayer structures, Phys. Rev. B **50**, 6094 (1994).

[21] T. Chiba, G. E. W. Bauer, and S. Takahashi, Magnetization damping in noncollinear spin valves with antiferromagnetic interlayer couplings, Phys. Rev. B **92**, 054407 (2015).

[22] D. O. Smith, Static and dynamic behavior of thin permalloy films, J. Appl. Phys. **29**, 264 (1958).

[23] G. Tatara, H. Kohno, and J. Shibata, Microscopic approach to current-driven domain wall dynamics, Phys. Rep. **468**, 213 (2008).

[24] L. D. Landau and E. M. Lifshitz, *Mechanics* (Butterworth-Heinemann, 1976), 3rd ed.

[25] M. van Kampen, C. Jozsa, J. Kohlhepp, P. LeClair, L. Lagae, W. de Jonge, and B. Koopmans, All-Optical Probe of Coherent Spin Waves, Phys. Rev. Lett. **88**, 227201 (2002).

[26] A. Kirilyuk, A. V. Kimel, and T. Rasing, Ultrafast optical manipulation of magnetic order, Rev. Mod. Phys. **82**, 2731 (2010).

[27] A. Barman, S. Wang, O. Hellwig, A. Berger, E. E. Fullerton, and H. Schmidt, Ultrafast magnetization dynamics in high perpendicular anisotropy $[\mathrm{Co/Pt}]_n$ multilayers, J. Appl. Phys. **101**, 09D102 (2007).

[28] S. Mizukami, F. Wu, A. Sakuma, J. Walowski, D. Watanabe, T. Kubota, X. Zhang, H. Naganuma, M. Oogane, Y. Ando, and T. Miyazaki, Long-Lived Ultrafast Spin Precession in Manganese Alloys Films with a Large Perpendicular Magnetic Anisotropy, Phys. Rev. Lett. **106**, 117201 (2011).

[29] S. Mizukami, A. Sugihara, S. Iihama, Y. Sasaki, K. Z. Suzuki, and T. Miyazaki, Laser-induced THz magnetization precession for a tetragonal heusler-like nearly compensated ferrimagnet, Appl. Phys. Lett. **108**, 012404 (2016).

[30] A. Kamimaki, S. Iihama, T. Taniguchi, and S. Mizukami, All-optical detection and evaluation of magnetic damping in synthetic antiferromagnet, Appl. Phys. Lett. **115**, 132402 (2019).

[31] Y. Tserkovnyak, A. Brataas, and G. E. W. Bauer, Enhanced Gilbert Damping in Thin Ferromagnetic Films, Phys. Rev. Lett. **88**, 117601 (2002).

[32] E. Beaurepaire, J.-C. Merle, A. Daunois, and J.-Y. Bigot, Ultrafast Spin Dynamics in Ferromagnetic Nickel, Phys. Rev. Lett. **76**, 4250 (1996).

[33] F. Dalla Longa, J. T. Kohlhepp, W. J. M. de Jonge, and B. Koopmans, Influence of photon angular momentum on ultrafast demagnetization in nickel, Phys. Rev. B **75**, 224431 (2007).

[34] Z. Zhang, L. Zhou, P. E. Wigen, and K. Ounadjela, Using Ferromagnetic Resonance as a Sensitive Method to Study Temperature Dependence of Interlayer Exchange Coupling, Phys. Rev. Lett. **73**, 336 (1994).

[35] N. Wiese, T. Dimopoulos, M. Ruhrig, J. Wecker, G. Reiss, J. Sort, and J. Nogues, Strong temperature dependence of antiferromagnetic coupling in CoFeB/Ru/CoFeB, Europhys. Lett. **78**, 67002 (2007).

[36] M. C. Weber, H. Nembach, B. Hillebrands, and J. Fassbender, Real-time temperature dynamics in exchange-biased bilayers upon laser excitation, IEEE Trans. Magn. **41**, 1089 (2005).

[37] F. Dalla Longa, J. T. Kohlhepp, W. J. M. de Jonge, and B. Koopmans, Laser-induced magnetization dynamics in Co/IrMn exchange coupled bilayers, J. Appl. Phys. **103,** 07B101 (2008).

[38] U. Atxitia, O. Chubykalo-Fesenko, N. Kazantseva, D. Hinzke, U. Nowak, and R. W. Chantrell, Micromagnetic modeling of laser-induced magnetization dynamics using the Landau-Lifshitz-Bloch equation, Appl. Phys. Lett. **91,** 232507 (2007).

[39] B. Koopmans, G. Malinowski, F. Dalla Longa, D. Steiauf, M. Fähnle, T. Roth, M. Cinchetti, and M. Aeschlimann, Explaining the paradoxical diversity of ultrafast laser-induced demagnetization, Nat. Mater. **9,** 259 (2010).

[40] J. Hamrle, J. Ferre, M. Nyvlt, and S. Visnovsky, In-depth resolution of the magneto-optical Kerr effect in ferromagnetic multilayers, Phys. Rev. B **66,** 224423 (2002).

[41] E. Goto, The parametron, a digital computing element which utilizes parametric oscillation, Proc. IRE **47,** 1304 (1959).

[42] P. Grunberg, Magnetostatic spin-wave modes of a heterogeneous ferromagnetic double layer, J. Appl. Phys. **52,** 6824 (1981).

[43] K. Di, S. X. Feng, S. N. Piramanayagam, V. L. Zhang, H. S. Lim, S. C. Ng, and M. H. Kuok, Enhancement of spin-wave nonreciprocity in magnonic crystals via synthetic antiferromagnetic coupling, Sci. Rep. **5,** 10153 (2015).

[44] R. A. Gallardo, T. Schneider, A. K. Chaurasiya, A. Oelschlägel, S. S. P. K. Arekapudi, A. Roldán-Molina, R. Hübner, K. Lenz, A. Barman, J. Fassbender, J. Lindner, O. Hellwig, and P. Landeros, Reconfigurable Spin-Wave Nonreciprocity Induced by Dipolar Interaction in a Coupled Ferromagnetic Bilayer, Phys. Rev. Appl. **12,** 034012 (2019).

[45] E. Albisetti, S. Tacchi, R. Silvani, G. Scaramuzzi, S. Finizio, S. Wintz, C. Rinaldi, M. Cantoni, J. Raabe, G. Carlotti, R. Bertacco, E. Riedo, and D. Petti, Optically inspired nanomagnonics with nonreciprocal spin waves in synthetic antiferromagnets, Adv. Mater. **1906439,** 1906439 (2020).

[46] M. Romera, P. Talatchian, S. Tsunegi, F. Abreu Araujo, V. Cros, P. Bortolotti, J. Trastoy, K. Yakushiji, A. Fukushima, H. Kubota, S. Yuasa, M. Ernoult, D. Vodenicarevic, T. Hirtzlin, N. Locatelli, D. Querlioz, and J. Grollier, Vowel recognition with four coupled spin-torque nano-oscillators, Nature **563,** 230 (2018).

[47] T. Kanao, H. Suto, K. Mizushima, H. Goto, T. Tanamoto, and T. Nagasawa, Reservoir Computing on Spin-Torque Oscillator Array, Phys. Rev. Appl. **12,** 024052 (2019).

[48] B. Heinrich, G. Woltersdorf, R. Urban, and O. Mosendz, Magnetic properties of NiMnSb(001) films grown on InGaAs/InP(001), J. Appl. Phys. **95,** 7462 (2004).

[49] C. Scheck, L. Cheng, I. Barsukov, Z. Frait, and W. E. Bailey, Low Relaxation Rate in Epitaxial Vanadium-Doped Ultrathin Iron Films, Phys. Rev. Lett. **98,** 117601 (2007).

[50] S. Mizukami, D. Watanabe, M. Oogane, Y. Ando, Y. Miura, M. Shirai, and T. Miyazaki, Low damping constant for Co_2FeAl Heusler alloy films and its correlation with density of states, J. Appl. Phys. **105,** 07D306 (2009).

[51] M. A. W. Schoen, D. Thonig, M. L. Schneider, T. J. Silva, H. T. Nembach, O. Eriksson, O. Karis, and J. M. Shaw, Ultra-low magnetic damping of a metallic ferromagnet, Nat. Phys. **12,** 839 (2016).

[52] S. Andrieu, A. Neggache, T. Hauet, T. Devolder, A. Hallal, M. Chshiev, A. M. Bataille, P. Le Fèvre, and F. Bertran, Direct evidence for minority spin gap in the Co_2MnSi Heusler compound, Phys. Rev. B **93,** 094417 (2016).

[53] S. Yakata, Y. Ando, T. Miyazaki, and S. Mizukami, Temperature dependences of spin-diffusion lengths of Cu and Ru layers, Jpn. J. Appl. Phys. **45,** 3892 (2006).

[54] J. Zak, E. R. Moog, C. Liu, and S. D. Bader, Universal approach to magneto-optics, J. Magn. Magn. Mater. **89,** 107 (1990).

[55] C.-Y. You and S.-C. Shin, Derivation of simplified analytic formulae for magneto-optical Kerr effects, Appl. Phys. Lett. **69,** 1315 (1996).

[56] J. J. Krebs, G. A. Prinz, D. W. Forester, and W. G. Maisch, Magneto-optical characterization of thin films of $Fe_{1-x}B_x$, $Fe_{1-x}Si_x$, and Fe-overcoated permalloy, J. Appl. Phys. **50,** 2449 (1979).

[57] T. J. Bright, J. I. Watjen, Z. M. Zhang, C. Muratore, A. A. Voevodin, D. I. Koukis, D. B. Tanner, and D. J. Arenas, Infrared optical properties of amorphous and nanocrystalline Ta_2O_5 thin films, J. Appl. Phys. **114,** 083515 (2013).

[58] M. A. Ordal, R. J. Bell, R. W. Alexander, L. A. Newquist, and M. R. Querry, Optical properties of Al, Fe, Ti, Ta, W, and Mo at submillimeter wavelengths, Appl. Opt. **27,** 1203 (1988).

[59] M. Yamamoto and T. Namioka, In situ ellipsometric study of optical properties of ultrathin films, Appl. Opt. **31,** 1612 (1992).

[60] X. Liang, X. Xu, R. Zheng, Z. A. Lum, and J. Qiu, Optical constant of CoFeB thin film measured with the interference enhancement method, Appl. Opt. **54,** 1557 (2015).

[61] I. H. Malitson, Interspecimen comparison of the refractive index of fused silica, J. Opt. Soc. Am. **55,** 1205 (1965).

[62] M. A. Green, Self-consistent optical parameters of intrinsic silicon at 300 K including temperature coefficients, Sol. Energy Mater. Sol. Cells **92,** 1305 (2008).

[63] M. L. Schneider, T. Gerrits, A. B. Kos, and T. J. Silva, Experimental determination of the inhomogeneous contribution to linewidth in Permalloy films using a time-resolved magneto-optic Kerr effect microprobe, J. Appl. Phys. **102,** 053910 (2007).